 SL, vol.9, no.1, pp.1-22, 2013

Numerical Analysis on the Interaction between Two Zipper Frac Wells with Continuum Damage Model

Xinpu Shen[1]

Abstract: Zipper fracturing ('zipper frac') is a popular reservoir stimulation method used to develop unconventional resources, particularly for tight sand oil, shale oil, and shale gas. Adequately understanding the influence of neighboring stimulation stages on generating the desired stimulated reservoir volume (SRV) has significant impact on fracturing design. To discover the mechanism of interaction between neighboring stimulation stages, numerical simulation was performed on the stimulation process step-by-step using the coupled hydro-mechanical Finite Element Method. A continuum damage model is used to simulate fracture phenomena created by fluid injection used for reservoir stimulation.

Numerical results presented here include: 1) distribution of the fracture volume shown with a contour of the continuum damage variable resulting from the injection flow; 2) pore pressure distribution corresponding to the end of a given stimulation stage; 3) contours of the horizontal stress components S-x and S-y.

A comparison of the numerical results of SRV indicates that for the zipper frac method, the SRV generated by sequential injection is narrow and significantly less than that generated by simultaneous injection. Numerical results also indicate that due to the changes in geostress field caused by the neighboring injection, the SRV created by stimulation in the central area of the submodel is much larger than that created at the corner locations. Calibration and modeling of the initial damage field also has significant impact on accurately modeling this multi-physics phenomenon and will be the major subject of the next step of this study.

Keywords: Continuum damage, stimulated reservoir volume, injection, zipper frac, tight sand.

1 Introduction

As a major measure of reservoir stimulation, hydraulic fracturing has been investigated since the 1950s [Christianovich and Zheltov (1955); Cleary (1980)]. As a

[1] Halliburton, USA.

result of the rapid development of unconventional petroleum resources in recent years, the investigation of hydraulic fracturing has attracted the interest of many researchers [Soliman, East, and Adams (2004); Ehlig-Economides, Valko and Dyashev (2006); Bagherian, Sarmadivale and Ghalambor et al (2010); Bahrami and Mortazavi (2008); Shaoul, van Zelm and de Pater (2011)].

Zipper fracturing ('zipper frac') is a popular reservoir stimulation method used to develop unconventional resources, particularly for tight sand oil, shale oil, and shale gas. Adequately understanding the influence of neighboring stimulation stages on generating the desired stimulated reservoir volume (SRV) has significant impact on fracturing design. To discover the mechanism of interaction between neighboring stimulation stages, numerical simulation was performed on the stimulation process step-by-step using the coupled hydro-mechanical Finite Element Method (FEM). A continuum damage model is used to simulate fracture phenomena created by fluid injection used for reservoir stimulation.

In rock mechanics, the mechanical damage variable is interpreted as an index of material continuity, which varies from 0 for intact rock to 1 for completely separated and broken rock. The volumetric density of cracks created by injection fluid can be represented by a scalar damage variable.

Submodeling techniques are used to accommodate the field-to-borehole-section scale discrepancy. The concept of the submodeling technique includes using a large-scale global model to produce boundary conditions for a smaller scale submodel. In this way, the hierarchical levels of the submodel are not limited. Using this approach, a highly inclusive field-scale analysis can be linked to a very detailed local-stress analysis at a much smaller scale. The benefits are bidirectional, with both the larger and smaller scale simulations benefiting from the linkage.

In the following sections, a plasticity-based damage model is introduced. A coupled calculation of hydro-mechanical problems with a 3D FEM performed in this paper is presented in Sections 3, 4, and 5. The numerical results for the distribution of mechanical variables, including continuum damage, pore pressure, and horizontal stress components, are analyzed and shown. Section 6 provides conclusions.

2 The damage model

The damage model used here was first proposed by Lubliner, Oliver, Oller et al. (1989), and was improved upon by Lee and Fenves (1998). This model is a plasticity-based scalar continuum damage model. The mechanism for the damage evolution in this model includes two aspects: damage resulting from tensile cracking and damage resulting from compressive crushing. The evolution of plastic loading is controlled by two hardening parameters: the equivalent plastic strain

$\bar{\varepsilon}_t^{pl}$ caused by the tensile load, and $\bar{\varepsilon}_c^{pl}$ caused by the compressive load.

2.1 Uniaxial behavior of the damage model

As shown in Figure 1(a), under tension the material shows linear elastic behavior before the stress reaches the value σ_{t_0}. A microcrack, which is modeled as a scalar damage variable, begins as the stress values exceed σ_{t_0}. Strain-softening phenomenon appears as a result of damage evolution, and results in strain localization in the structure.

For compressive behavior as shown in Figure 1(b), the material also shows linear elastic behavior before the stress reaches the value σ_{c0}. Microcrack/damage begins as the stress values exceed σ_{c_0}. Strain-hardening appears and lasts until the stress level reaches σ_{cu}. As the stress level exceeds σ_{cu}, the strain-softening phenomenon appears as a result of damage evolution, and results in strain localization in the structure.

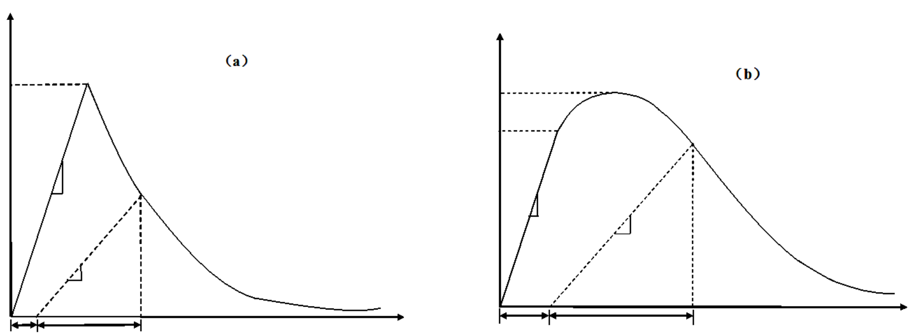

Figure 1: Uniaxial behavior of the model: (a) under tension; (b) under compression.

Because of damage initiation and evolution, unloading stiffness is degraded from its original value of the intact material, as shown in Figure 1. This stiffness degradation is expressed in terms of two damage variables: d_t and d_c. The value of the damage variables are 0 for the intact material and 1 for the completely broken state.

Assuming that E_0 is the Young's modulus of the initial intact material, the Hooke's law under uniaxial loading conditions is:

$$\sigma_t = (1 - d_t)E_0(\varepsilon_t - \bar{\varepsilon}_t^{pl}) \quad (1)$$

$$\sigma_c = (1 - d_c)E_0(\varepsilon_c - \bar{\varepsilon}_c^{pl}) \quad (2)$$

Therefore, the effective stress for tension and compression can be written as:

$$\bar{\sigma}_t = \frac{\sigma_t}{1-d_t} = E_0(\varepsilon_t - \bar{\varepsilon}_t^{pl}) \tag{3}$$

$$\bar{\sigma}_c = \frac{\sigma_c}{1-d_c} = E_0(\varepsilon_c - \bar{\varepsilon}_c^{pl}) \tag{4}$$

Plastic yielding criteria will be described in the space of effective stress.

2.2 Unloading behavior

A description of the unloading behavior of the model is important for the application of the model to periodic loading conditions. The closure and opening of the microcracks will result in significant nonlinearity of the material behavior. It is experimentally proved that crack closure will result in some degree of stiffness recovery, which is also known as the 'unilateral effect'.

The relationship of Young's modulus $E$for damaged material and that of the intact material $E_0$is:

$$E = (1-d)E_0 \tag{5}$$

Lemaitre's 'strain equivalent assumption' is adopted in this paper. In Eq. 5, d is the synthetic damage variable, which is a function of stress state s, tensile damage d_t, and compressive damage d_c, and can be expressed as:

$$(1-d) = (1-s_t d_c)(1-s_c d_t) \tag{6}$$

where s_t and s_c are functions of the stress state and are calculated as follows:

$$s_t = 1 - w_t \gamma^*(\sigma_{11})\ ; \qquad 0 \le w_t \le 1 \tag{7}$$

$$s_c = 1 - w_c(1-\gamma^*(\sigma_{11}))\ ; \qquad 0 \le w_c \le 1 \tag{8}$$

In Eq. 7, $\gamma^*(\sigma_{11}) = H(\sigma_{11}) = \begin{cases} 1 & \text{as} \quad \sigma_{11} > 0 \\ 0 & \text{as} \quad \sigma_{11} < 0 \end{cases}$.

The weight parameters, w_t and w_c, are the material properties that control the amount of stiffness recovery for the unloading process, as shown in Figure 2.

Hooke's law at the triaxial stress state is expressed in the following tensor form:

$$\sigma = (1-d)\mathbf{D}_0^{el} : (\varepsilon - \varepsilon^{\mathbf{pl}}) \tag{9}$$

where $\mathbf{D}_0^{el}$ is the matrix of stiffness of the intact materials. At a triaxial stress state, the Heaviside function in the expression of the synthetic damage variable d can be written as:

$$\gamma(\hat{\sigma}) = \frac{\sum_{i=1}^{3} < \sigma_i >}{\sum_{i=1}^{3} |\hat{\sigma}_i|} \quad ; \quad 0 \leq \gamma(\hat{\sigma}) \leq 1 \tag{10}$$

where $\hat{\sigma}_i$ $(i = 1,2,3)$ is the principal stress components, and the symbol $< \cdot >$ indicates that $< \chi >= \frac{1}{2}(|\chi| + \chi)$.

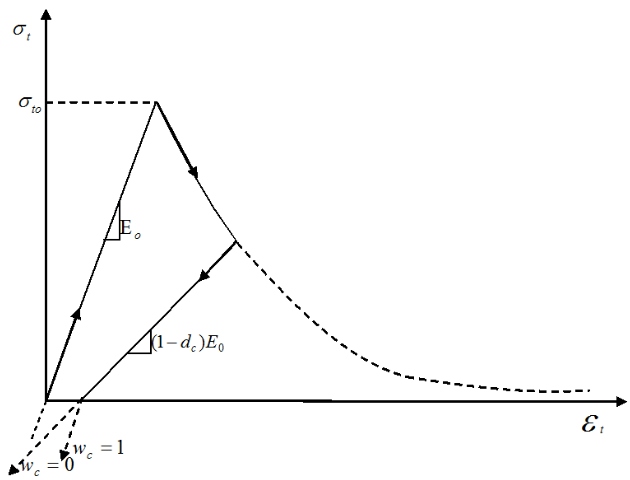

Figure 2: The unloading behavior of the Barcelona model.

2.3 Plastic flow

The non-associated plastic flow rule is adopted in this model. The plastic potential G is in the form of a Drucker-Prager type and is expressed as:

$$G = \sqrt{(\varepsilon\,\sigma_{t0} tg\psi)^2 + \bar{q}^2} - \bar{p} tg\psi \tag{11}$$

where $\psi(\theta, f_i)$ is the dilatancy angle and $\sigma_{t0}(\theta, f_i) = \sigma_t|_{\bar{\varepsilon}_t^{pl}=0}$ is the threshold value of the tensile stress at which damage initiates. Parameter $\varepsilon(\theta, f_i)$ is a model parameter that defines the eccentricity of the loading surface in the effective stress space.

2.4 Yielding criterion

The yielding criterion of the model is given in the effective stress space and its evolution is determined by two variables $\bar{\varepsilon}_t^{pl}$ and $\bar{\varepsilon}_c^{pl}$. Its expression is provided in

Eq. (12):

$$F = \frac{1}{1-\alpha}(\bar{q} - 3\alpha\bar{p} + \beta(\bar{\varepsilon}^{pl}) < \hat{\bar{\sigma}}_{\max} > -\gamma < -\hat{\bar{\sigma}}_{\max} >) - \bar{\sigma}_c(\bar{\varepsilon}_c^{pl}) = 0 \tag{12}$$

where

$$\begin{aligned} \alpha &= \frac{(\sigma_{b0}/\sigma_{c0}) - 1}{2(\sigma_{b0}/\sigma_{c0}) - 1}, \quad 0 \leq \alpha \leq 0.5, \\ \beta &= \frac{\bar{\sigma}_c(\bar{\varepsilon}_c^{pl})}{\bar{\sigma}_t(\bar{\varepsilon}_t^{pl})}(1-\alpha) - (1+\alpha). \quad \gamma = \frac{3(1-k_c)}{2k_c - 1} \end{aligned} \tag{13}$$

And where $\hat{\bar{\sigma}}_{\max}$ is the value of the maximum principal stress component and σ_{b0}/σ_{c0} is the ratio between the limit of bi-axial compression and uniaxial compression. Parameter k_c is the ratio between the second invariant of the stress tensor at the tensile meridian $q(TM)$ and the second invariant at the compressive meridian $q(CM)$ under arbitrary pressure, which means $\hat{\sigma}_{\max} < 0$. It is also required that $0.5 < k_c \leq 1.0$, with a default value of 2/3. In Eq. 12, $\bar{\sigma}_t(\bar{\varepsilon}_t^{pl})$is the effective tensile strength and $\bar{\sigma}_c(\bar{\varepsilon}_c^{pl})$ is the effective compressive strength. Figure 3shows the yielding surface for various values of k_c at πplane. Figure 4 shows the yielding surface for the plane-stress state.

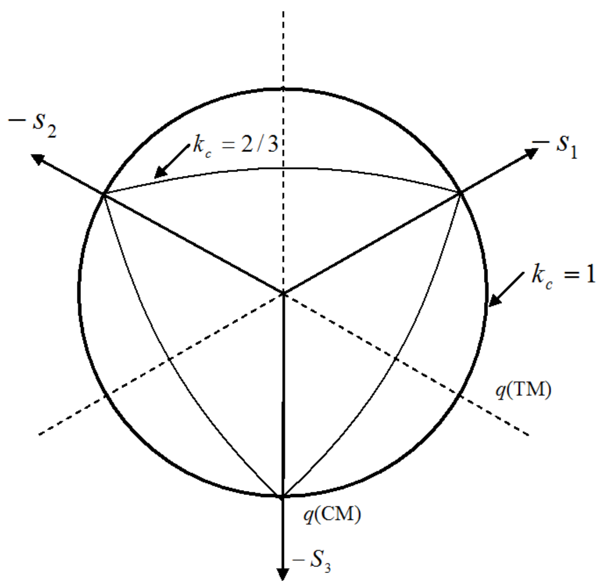

Figure 3: The yielding surface for various values of k_c at π plane.

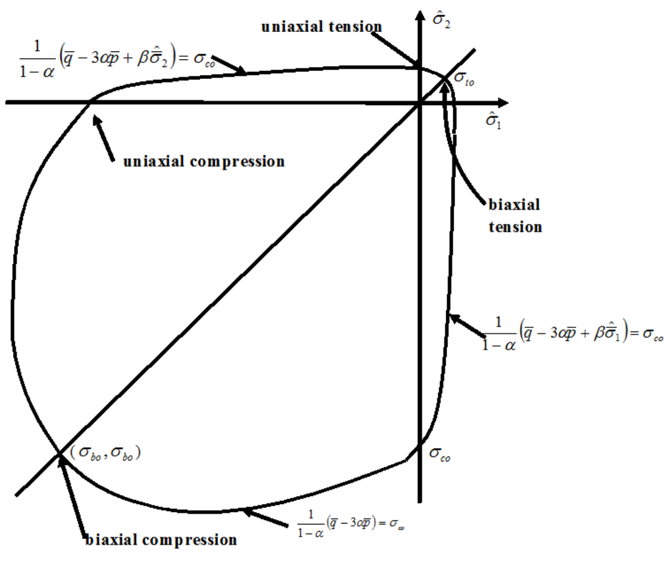

Figure 4: The yielding surface for plane stress state.

3 The field model

3.1 Model geometry

Figure 5 shows the field scale model geometry. The following factors indicate the model definition: the X-direction of the model is chosen as the direction of the maximum principal stress, which has an azimuth angle of NE14°.

The scale of the model consists of the following: both the width and length are 10 km, and the thickness/depth is 6 km. The top of the wellbore is in the center of the model. The inclination angle of the formation sediment layer is set as 6.5°. A 5000 C3D20RP element was used to discretize the field model.

3.2 Loads and boundary conditions of the global model

Figure 5 shows the boundary conditions. The key characteristics of the boundary sets include the following:

- Normal displacement constraints are applied to all lateral surfaces and the bottom surface. The top surface is set as a free surface.
- Simplification has been adopted here; the variation of the elevation of the top surface is neglected.

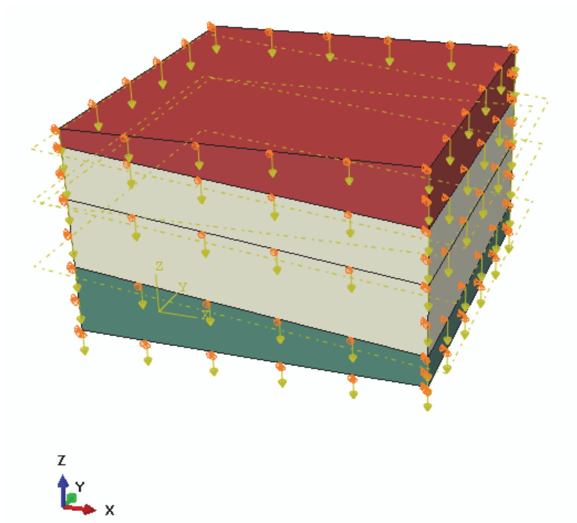

Figure 5: Loads and boundary conditions of the global model.

3.3 Initial conditions

Parameters for the initial conditions defined for the model include the following:

- The initial geostress field is applied with an effective stress ratio of k0=0.6 and a tectonic factor, tf=0.5. This initial value will be balanced with the gravity load of the formations and will be automatically modified by equilibrium equations.
- Initial pore pressure is applied to the formations.

3.4 Loads

The types of loads applied to the model include the following:

- A gravity load is applied to the model.
- This gravity will be used to balance the initial geostress field with pore pressure.

4 Numerical results of the global model

With the model definition provided in Section 3, a coupled numerical simulation was performed for the geostress field and for pore pressure initialization of the given field. Visualization of the directions of the principal stresses in the form of sectional views in the X-Y plane are shown in Figure 6. The results are sectional views taken at TVD=1700 m. From top to bottom, the variables shown in Figure 6 are: 1) maximum compressive stress, 2) medium compressive stress, and 3) minimum compressive stress.

This set of numerical results of the global model at the field scale provides boundary conditions to the local model, which will be used to simulate the stimulation process, as described in Section 5.

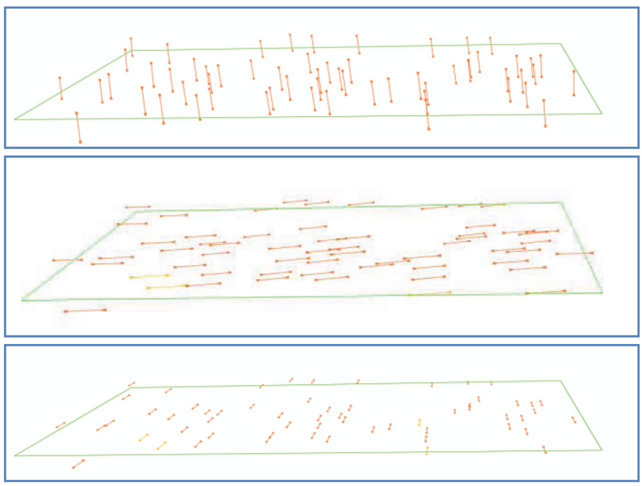

Figure 6: 3D global model—visualization of the principal directions of the stress tensors.

5 Submodel for stimulation process simulation

5.1 Definition of the Submodel under Stimulation Injection Loadings

The submodel geometry is 200 m in width and length, and has a thickness of 20 m. The calculation is focused on the lateral scope of the fractured volume generated by fluid injection. Therefore, the vertical direction of the mode has been simplified by taking just a thin slice shape in 3D space.

Figure 7 shows the horizontal well section design for the zipper frac process. 7,560 3D 8-noded continuum elements (C3D8RPH) are used in discretization of the model. Figure 8 shows the mesh of the submodel.

The load under the initial geostress is the injection flow at the injection points of the

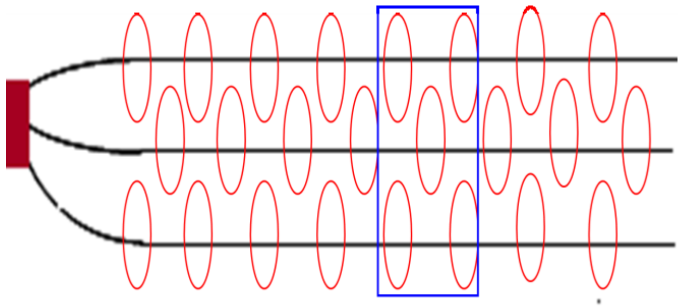

Figure 7: The parallel, horizontal well section design for the zipper frac process.

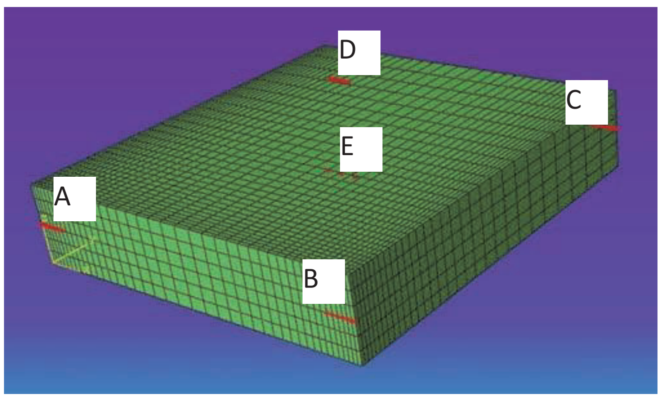

Figure 8: Mesh and geometry of the submodel.

submodel. The red points in Figure8 show the locations of the injection points. Due to the symmetrical nature of the model, only a quarter of the model was meshed. All four side surfaces are symmetrical planes.

The purpose of this calculation is to estimate the injection effects using the aforementioned parameter values for the zipper fracture of two horizontal wells. Injection points are located at the four corners and at the center of the model (red points shown in Figure 8). The length of the perforation section is 20 m. Due to the symmetrical nature of the geometric model, only 10 m of the perforation section is modeled with the injection points. The flow rate is the controlled loading variable which is given as known, and the pressures at the injection points are variable, are solved as unknown, and change with the injection process.

Numerical simulation of each of the injection steps at the five locations (see Figure 8) for the injection loading case will be simulated one after another. This replicates the stimulation process as practiced in the field.

This calculation will simulate fracture generation under a bottom-hole pressure (Btmh) of 5730 psi, along with the following conditions:

- Reservoir initial pore pressure of 3000 psi, corresponding to TVD = 1700 m.
- Boundary conditions from the numerical results of the global model described in Section 3.
- Initial geostress values from the numerical results of the global model described in Section 3, corresponding to TVD = 1700 m.

5.2 Numerical results of the submodel under stimulation injection loadings

Using the aforementioned submodel, the stimulation processes are numerically simulated.

To investigate the interaction of fracture zones created by stimulation injection, the loading sequence of the injection was set as:

- 1^{st} stage: injection loading at location A
- 2^{nd} stage: injection loading at location B
- 3^{rd} stage: injection loading at location C
- 4^{th} stage: injection loading at location D
- 5^{th} stage: injection loading at location E

Figure 9 to Figure 12 present the resulting contours of major mechanical variables at the end of the 1^{st} stage. Figure 9 shows the pore pressure distribution in the submodel corresponding to the end of the 1st stage at location A. Figure10 shows the fractured reservoir volume which is a rather narrow band in 3D space. Figure 11 shows the distribution of the horizontal stress component S-x in the x-direction. These stress components are all effective stresses whose amount is the result of total stress minus pore pressure. Figure12 shows another horizontal stress component, S-y, in the y-direction. The variation of the vertical stress component S-z is simply the resultant of amount of total vertical stress minus pore pressure; therefore, it is omitted here for purposes of brevity.

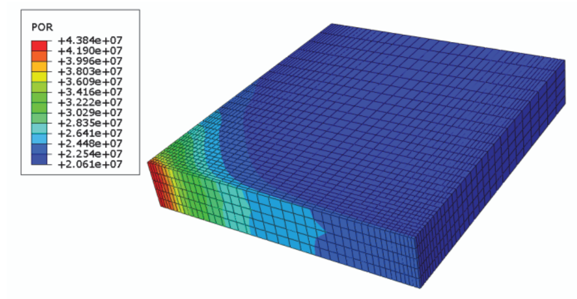

Figure 9: Pore pressure distribution of the submodel after the 1st stage injection stimulation.

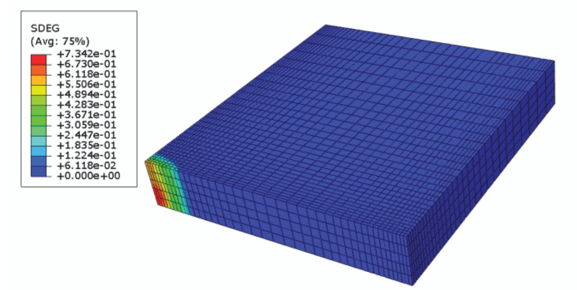

Figure 10: Fractured volume at 1st stage, distribution of continuum damage.

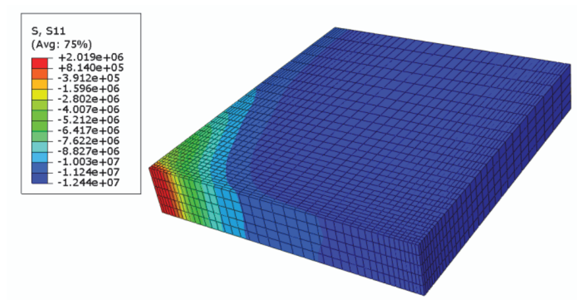

Figure 11: Contour of stress component S-x which is effective stress in the x-direction.

Figure 13 to Figure 16 present the resulting contours of major mechanical variables at the end of the 2^{nd} stage stimulation injection. Figure 13 shows the pore pressure distribution in the submodel corresponding to the end of the 2nd stage at location B. Figure14 shows the fractured reservoir volume which is also narrow.

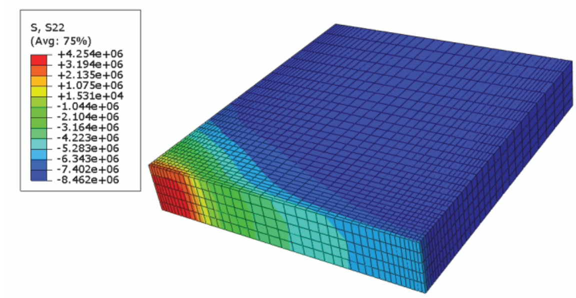

Figure 12: Contour of stress component S-y which is effective stress in the y-direction.

We can also see that the pore pressure near point A becomes smaller and smaller, but both its fractured volume and the value of the continuum damage variable get bigger and bigger due to the residual injection energy at this region degrading with time. Figure 15 shows the distribution of the horizontal stress component S-x in the x-direction. Figure16 shows another horizontal stress component, S-y, in the y-direction.

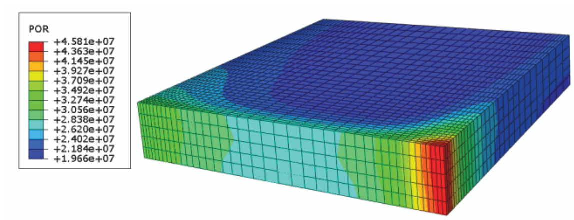

Figure 13: Pore pressure distribution of the submodel after 2nd stage injection stimulation.

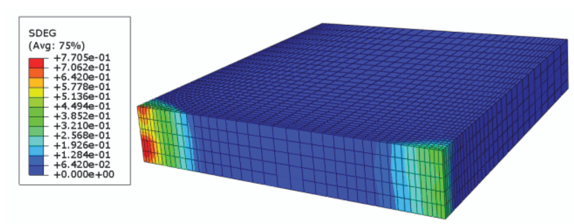

Figure 14: Fractured volume at 2nd stage, distribution of continuum damage.

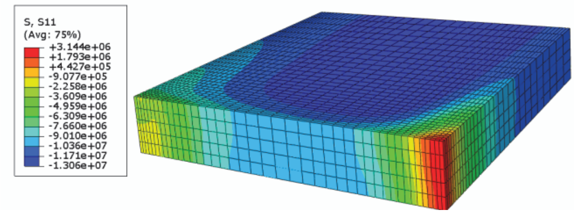

Figure 15: Contour of stress component S-x which is effective stress in the x-direction.

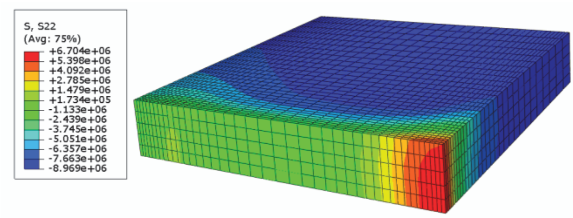

Figure 16: Contour of stress component S-y which is effective stress in the y-direction.

Figure 17 to Figure 20 present the resulting contours of major mechanical variables at the end of the 3^{rd} stage stimulation injection. Figure 17 shows the pore pressure distribution in the submodel corresponding to the end of injection of the 3^{rd} stage at location C. Figure 18 shows the fractured reservoir volume. Although it is still narrow, now the fracture volumes created by injection at location A and B respectively are connected, which means 'the fractured volume are zipped now'. Figure 19 shows the distribution of the horizontal stress component S-x in the x-direction. Figure 20 shows another horizontal stress component, S-y, in the y-direction. To show the internal distribution of the mechanical variables, multi-cut views are used in the visualization of these figures.

Figure 21 to 24 present the resulting contours of the major mechanical variables at the end of the 4^{th} stage stimulation injection. Figure 21 shows the pore pressure distribution in the submodel corresponding to the end of the 4^{th} stage at location D. Figure 22 shows the fractured reservoir volume. We can see that all four fractured volumes are now 'zipped'. Figure 23 shows distribution of the horizontal stress component S-x in the x-direction. Figure 24 shows another horizontal stress component, S-y, in the y-direction.

Figure 25 to Figure 28 show the resulting contours of the major mechanical variables at the end of the 5^{th} stage stimulation injection. Figure 25 shows the pore

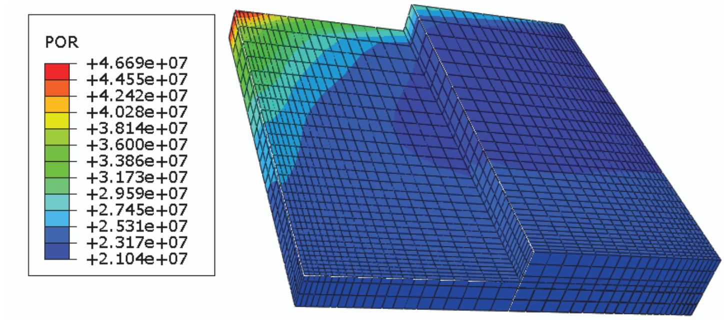

Figure 17: Pore pressure distribution of the submodel after 3rd stage injection stimulation.

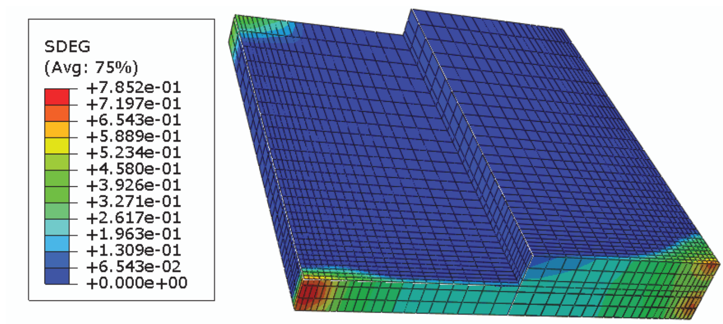

Figure 18: Fractured volume at 3rd stage, distribution of continuum damage.

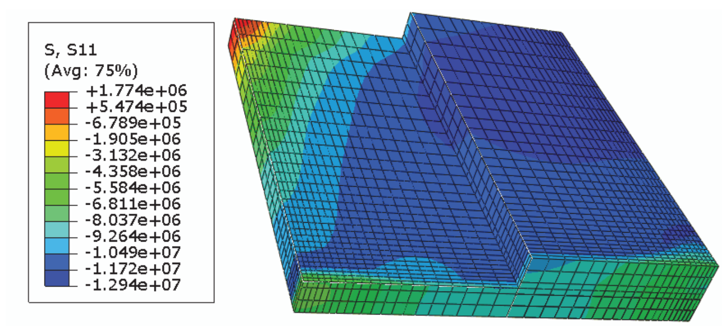

Figure 19: Contour of stress component S-x which is effective stress in the x-direction.

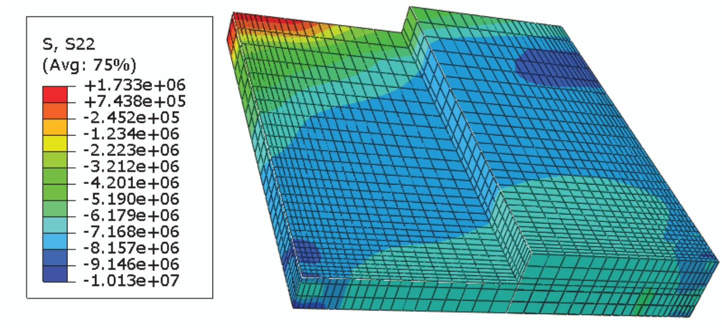

Figure 20: Contour of stress component S-y which is effective stress in the y-direction.

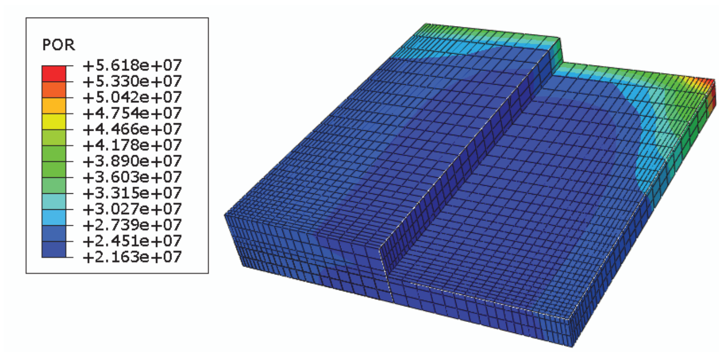

Figure 21: Pore pressure distribution of the submodel at 4th stage injection stimulation.

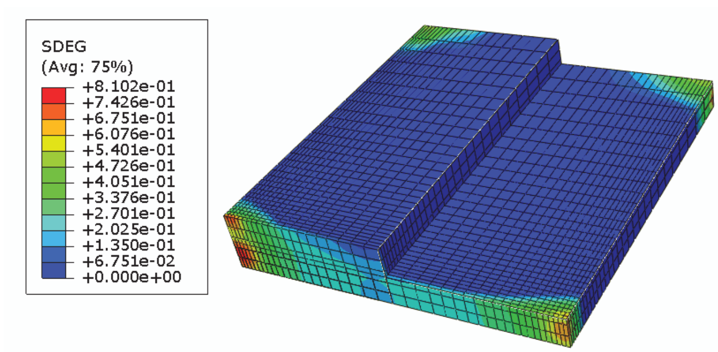

Figure 22: Fractured volume at 4th stage, distribution of continuum damage.

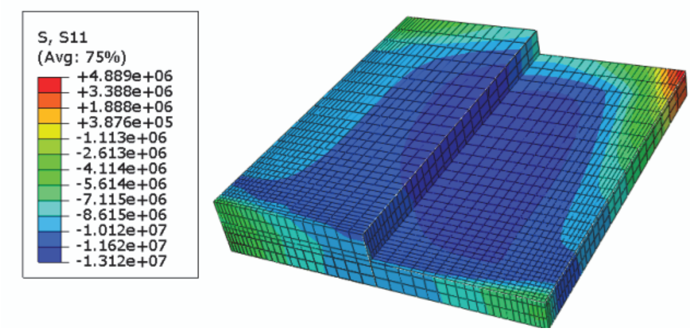

Figure 23: Contour of stress component S-x which is effective stress in the x-direction.

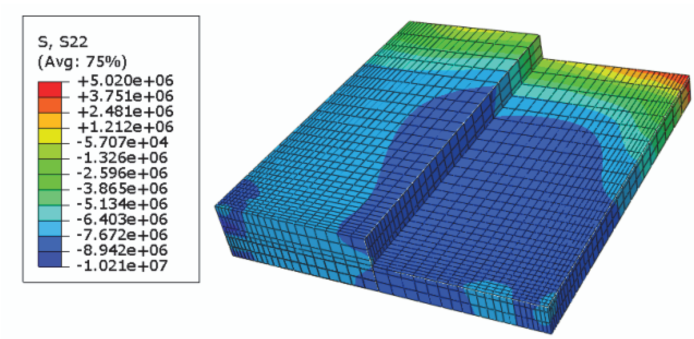

Figure 24: Contour of stress component S-y which is effective stress in the y-direction.

pressure distribution in the submodel corresponding to the end of the 5^{th} stage at location E. Figure 26 shows the fractured reservoir volume. We can see that the fractured reservoir volumes created by this injection stimulation are significantly larger than those created by previous stimulation steps using approximately the same injection pressure. Figure 27 shows distribution of the horizontal stress component S-x in the x-direction. Figure 28 shows another horizontal stress component, S-y, in the y-direction.

Figure 29 to Figure 32 show the resulting contours of the major mechanical variables after using a different stimulation injection method. In this case, two stimulation injections start simultaneously at both location A and location B, instead of one after another. Figure 29 shows the pore pressure distribution in the submodel corresponding to the simultaneous injection method. Figure 30 shows the fractured reservoir volume created by this case. We can see that the fractured volume is

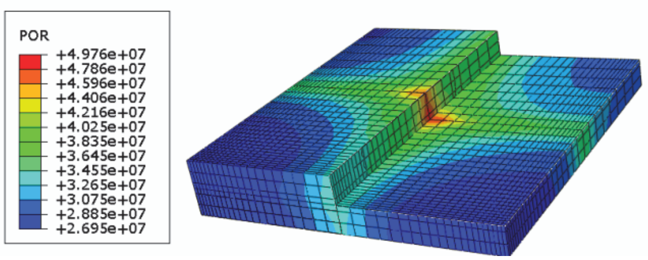

Figure 25: Pore pressure distribution of the submodel after 5th stage injection stimulation.

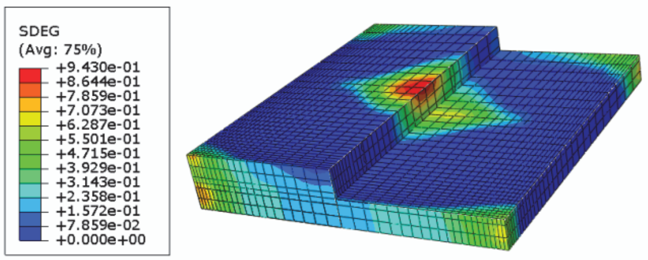

Figure 26: Fractured volume at 5th stage, distribution of continuum damage.

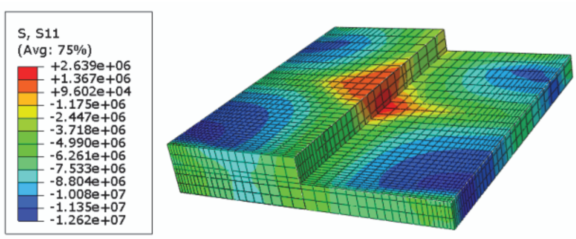

Figure 27: Contour of stress component S-x which is effective stress in the x-direction.

significantly wider than the one shown in Figure 10 and Figure 14 with approximately the same injection pressure. This indicates that the same injection pressure produces more fractured reservoir volume when the injections are simultaneous injection than when the injections are sequential during zipper frac. Figure 31 shows distribution of the horizontal stress component S-x in the x-direction. Figure 32 shows another horizontal stress component, S-y, in the y-direction.

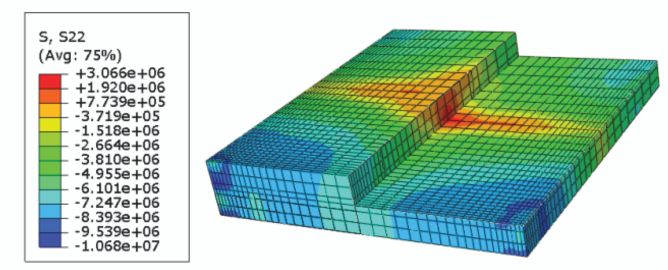

Figure 28: Contour of stress component S-y which is effective stress in the y-direction.

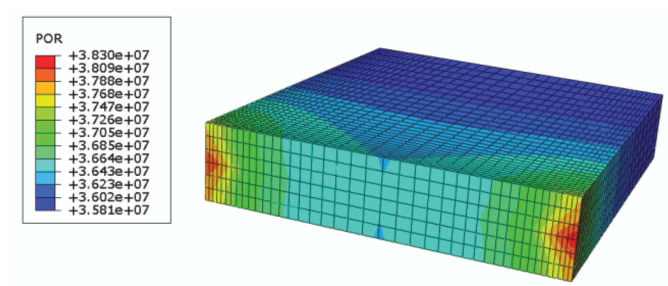

Figure 29: Pore pressure distribution of the submodel after simultaneous injection stimulation.

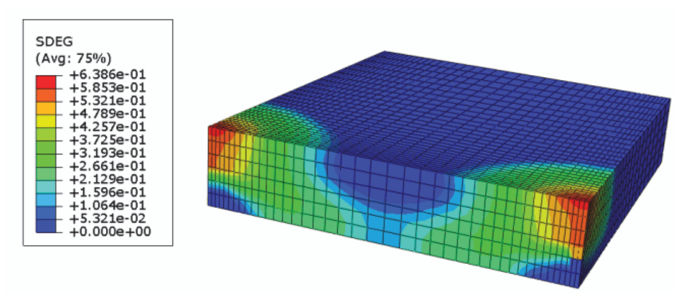

Figure 30: Fractured volume with simultaneous injection stimulation, distribution of continuum damage.

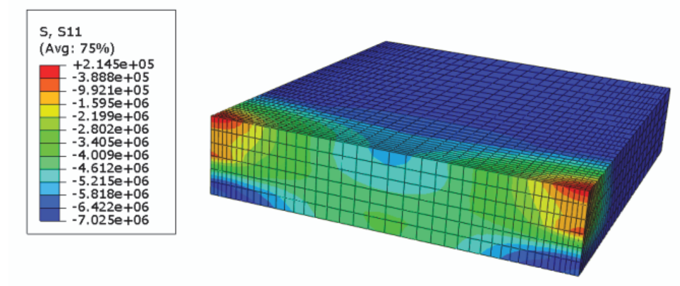

Figure 31: Contour of stress component S-x which is effective stress in the x-direction.

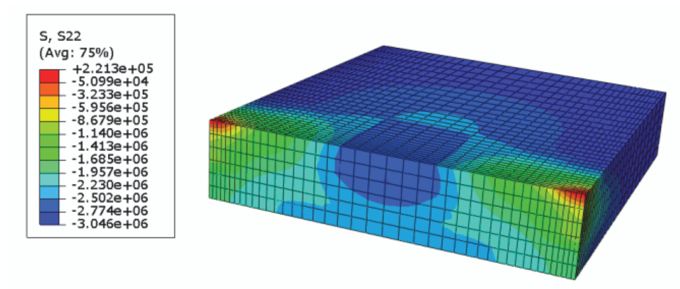

Figure 32: Contour of stress component S-y which is effective stress in the y-direction.

6 Conclusions

Zipper fracturing ('zipper frac') is a popular reservoir stimulation method used to develop unconventional resources, particularly for tight sand oil, shale oil, and shale gas. Adequately understanding the influence of neighboring stimulation stages on generating the desired stimulated reservoir volume (SRV) has significant impact on fracturing design. To discover the mechanism of interaction between neighboring stimulation stages, numerical simulation was performed on the stimulation process step-by-step using the coupled hydro-mechanical Finite Element Method. A continuum damage model is used to simulate fracture phenomena created by fluid injection used for reservoir stimulation.

Numerical results presented here include:

- distribution of the fractures shown with a contour of the continuum damage variable resulting from the injection flow

- pore pressure distribution corresponding to the end of a given stimulation stage
- contours of the horizontal stress components S-x and S-y

A comparison of the numerical results for SRV shown in Figure 10 and Figure 14 indicates that for zipper frac, the SRV generated by the sequential injection method is narrow and is significantly less than that generated by the simultaneous injection method.

The numerical results for SRV shown in Figure 26 indicate that due to the changes in the geostress field caused by the neighboring injection, SRV created by stimulation at the central area of this submodel is much larger than that created at the corner locations.

Data on the anisotropic distribution of permeability and the distribution of natural fractures are necessary to provide a solution which is closer to the measured fracture distribution data obtained with micro-seismic monitoring. Calibration of the damage model with micro-seismic data will be the major subject of the next step of this study. Calibration and modeling of the initial damage field also has significant impact on accurately modeling this multi-physics phenomenon.

References

Bagherian, B.; Sarmadivaleh, M.; Ghalambor, A.; Nabipour, A.; Rasouli, V.; Mahmoudi. M. (2010): Optimization of multiple-fractured horizontal tight gas well. *SPE International Symposium and Exhibition on Formation Damage Control,* Lafayette, Louisiana, USA, 10-12 February.

Bahrami, V.; A. Mortazavi. (2008): A numerical investigation of hydraulic fracturing process in oil reservoirs using non-linear fracture mechanics. *5th Asian Rock Mechanics Symposium,* Tehran, Iran, 24-26 November.

Christianovich, S. A.; Zheltov, Y. P. (1955): Formation of vertical fractures by means of a highly viscous fluid. *Proc. 4th World Petroleum Congress*, vol. 2, pp. 579-586.

Cleary, M. P. (1980): Comprehensive design formulae for hydraulic fracturing. *SPE Annual Technical Conference and Exhibition*, Dallas, Texas, USA, 21-24 September.

Ehlig-Economides, C.A.; Valko, P.; Dyashev, I. (2006): Pressure transient and production data analysis for hydraulic fracture treatment evaluation. *Russian Oil and Gas Technical Conference and Exhibition*, Moscow, Russia, 3-6 October.

Lee, J.; Fenves, G. L. (1998): Plastic-damage model for cyclic loading of concrete structures. *ASCE J. Engng Mech.* vol. 124, no. 8, pp. 892-900.

Lubliner, J.; Oliver, J.; Oller, S.; Onate, E. (1989): A plastic damage model for concrete. *Int. J. Solids & Struct.*, vol. 25, no. 3, pp. 299-326.

Shaoul, J.; Lars van Zelm; Pater, C. J. (2011): Damage mechanisms in unconventional-gas-well Stimulation–a new look at an old problem. *SPE Production & Operations*, vol. 26, no. 4, pp. 388-400.

Soliman, M. Y.; East, L.; Adams, D. (2004): Geo-mechanics aspects of multiple fracturing of horizontal and vertical wells. *SPE International Thermal Operations and Heavy Oil Symposium and Western Regional Meeting*, Bakersfield, California, USA, 16-18 March.